Anion photoelectron spectroscopy of B_2N^-

Knut R. Asmis, Travis R. Taylor, and Daniel M. Neumark[a)]
Department of Chemistry, University of California, Berkeley, and Chemical Sciences Division, Lawrence Berkeley National Laboratory, Berkeley, California 94720

(Received 3 August 1999; accepted 20 August 1999)

Vibrationally resolved 355 and 266 nm anion photoelectron spectra of B_2N are presented. Photodetachment to two electronic states of linear B–N–B is observed and, aided by electronic structure calculations, assigned to the $\tilde{X}\,^1\Sigma_g^+ \rightarrow \tilde{X}\,^2\Sigma_u^+ + e^-$ and $\tilde{X}\,^1\Sigma_g^+ \rightarrow \tilde{A}\,^2\Sigma_g^+ + e^-$ transitions. The electron affinity of B_2N is 3.098 ± 0.005 eV and the $\tilde{A}\,^2\Sigma_g^+$ term energy T_0 is 0.785 ± 0.005 eV. Observation of excitations involving uneven quanta of the antisymmetric stretching mode (ν_3) indicates a breakdown of the Franck–Condon (FC) approximation and results from Herzberg–Teller vibronic coupling between the $\tilde{X}\,^2\Sigma_u^+$ and $\tilde{A}\,^2\Sigma_g^+$ states involving the ν_3 mode. Measurement of the angular dependence of the photodetached electrons serves as a sensitive probe for the identification of these FC forbidden transitions. A linear vibronic coupling model qualitatively reproduces the perturbed ν_3 potentials of the $\tilde{X}$ and $\tilde{A}$ states. Artifactual symmetry breaking along the ν_3 coordinate is observed in the *ab initio* wave functions for the neutral ground state up to the coupled-cluster level of theory, even when Brueckner orbitals are used. No evidence is found for an energetically low-lying cyclic state of B_2N, which has been invoked in the assignment of the matrix infrared spectrum of B_2N. However, the matrix infrared data agrees well with the peak spacing observed in the photoelectron spectra and reassigned to the linear $\tilde{X}\,^2\Sigma_u^+$ ground state. © *1999 American Institute of Physics.* [S0021-9606(99)00743-6]

I. INTRODUCTION

Boron nitride thin films have received considerable attention in material science, due to the favorable properties these films exhibit for industrial applications.[1] Boron nitride clusters play an important role as precursors in the formation of these films. However, except for diatomic BN, which has been studied experimentally in some detail,[2–10] experimental and theoretical studies on the electronic structure of boron nitride species remains scarce. B_2N, BN_2, B_2N_2 and BN_3 have been identified by matrix isolation spectroscopy aided by *ab initio* calculations.[11–14] B_2N, as well as its singly charged ions, are formed upon laser vaporization of solid boron nitride.[12,15,16] B_2N can also be synthesized by reaction of pulsed laser produced B and N atoms.[12] We recently presented preliminary results on the first gas-phase spectroscopic studies on B_2N^-/B_2N and B_3N^-/B_3N using anion photoelectron spectroscopy.[17] Here we present a more detailed experimental investigation, aided by electronic structure calculations, of the spectroscopy and energetics of B_2N^- and B_2N.

There is considerable controversy in the literature concerning the geometry of B_2N. Matrix electron spin resonance spectroscopy found a linear B–N–B radical with $D_{\infty h}$ symmetry.[11] On the other hand, the dominant absorption in the matrix infrared (IR) spectrum of B_2N, characterized by an intense fundamental at 882.3 cm^{-1}, was assigned by Andrews and co-workers to a cyclic B_2N radical with C_{2v} symmetry.[12–14] A cyclic $^2B_2$ ground state is found at the unrestricted Hartree–Fock (UHF) level of theory, while more highly correlated methods predict a linear B–N–B ground state ($^2\Sigma_{(u)}^+$).[11,12,18] However, the complete-active-space self-consistent-field (CASSCF) wave function for the $^2\Sigma_u^+$ state is unstable with respect to symmetry lowering and calculations at this level predict a linear B–N––B species with unequal bond lengths.[19] Similar to the isoelectronic C_3^+, in which a linear isomer is predicted to lie 4–7 kcal/mol above the cyclic ground state,[20,21] the calculated ground state geometry of B_2N is very much dependent on the electron correlation treatment used.

In our previous photoelectron spectroscopy study (at 266 nm) of B_2N^-, we observed photodetachment from the anion to two electronic states of B_2N.[17] The electron affinity (EA) of B_2N was determined and preliminary assignments of the spectral features were given assuming linear, symmetric B–N–B structures for both the anion and the neutral. The photoelectron spectra are characterized by rich structure, but a detailed assignment of the observed vibrationally resolved features was not possible at that time. In this paper, photoelectron spectra and photoelectron angular distributions of B_2N^- at 355 and 266 nm are presented. We also examine the electronic structure of low-lying states of B_2N^- and B_2N using coupled cluster theory and density functional theory. The combination of the more detailed experimental results with the theoretical work enables us to resolve the controversy concerning the geometry of B_2N. Specifically, we find no evidence for an energetically low-lying cyclic isomer of B_2N. The matrix IR data agree with the peak spacing observed in the photoelectron spectra and is reassigned to the $\tilde{X}\,^2\Sigma_u^+$ ground state of linear B–N–B.

a)Electronic mail: dan@radon.cchem.berkeley.edu

II. EXPERIMENT

The negative ion tandem time-of-flight (TOF) photoelectron spectrometer used in this study has been described previously.[22,23] Boron nitride clusters are prepared by laser ablation with the second harmonic (532 nm, 20–30 mJ/pulse) of a Nd:YAG laser tightly focused onto a rotating and translating ''hot-pressed'' boron nitride disk (Carborundum Corp.). The resulting plasma is entrained in a pulse of Ar carrier gas and expanded through a clustering channel. Ions formed in the expansion are extracted perpendicularly to the expansion by means of a pulsed electric field and accelerated to a beam energy of 1.25 keV. The extracted ions enter a linear reflectron TOF mass spectrometer, where they separate in time and space according to their mass-to-charge ratios. The mass resolution is $m/\Delta m \approx 2000$. At the spatial focus of the mass spectrometer, photoelectrons are detached from the mass-selected ions by a fixed frequency laser pulse from a second Nd:YAG laser. The laser firing delay is varied until optimal temporal overlap is achieved with ions of desired mass. The third (355 nm, 3.493 eV, ~140 mJ/cm^2) and fourth harmonics (266 nm, 4.657 eV, ~70 mJ/cm^2) of the second laser were used in this study. The instrument is operated at a repetition rate of 20 Hz. The photoelectron kinetic energy (eKE) is determined by field-free TOF in a 1 m flight tube. All photoelectron spectra presented here are plotted as a function of the electron binding energy (eBE) defined as

$$e\mathrm{BE} = h\nu - e\mathrm{KE} = \mathrm{EA} + E_{\mathrm{int}}^{(0)} - E_{\mathrm{int}}^{(-)}, \quad (1)$$

where $h\nu$ denotes the photon energy of the detachment laser, EA the electron affinity of the neutral, and $E_{\mathrm{int}}^{(0)}$ and $E_{\mathrm{int}}^{(-)}$ the internal energies of the neutral and the anion, respectively.

This apparatus also yields the angular distribution of the detached photoelectrons, which is given by

$$\frac{d\sigma}{d\Omega} = \frac{\sigma_{\mathrm{tot}}(e\mathrm{KE})}{4\pi}\left[1 + \frac{\beta(e\mathrm{KE})}{2}(3\cos^2\theta - 1)\right], \quad (2)$$

where $\sigma_{\mathrm{tot}}(e\mathrm{KE})$ is the total photodetachment cross section, $\beta(e\mathrm{KE})$ is the asymmetry parameter ($-1 \leqslant \beta \leqslant 2$), and θ is the angle between the direction of the ejected electron and the polarization of the incident light.[24] θ is varied by means of a 1/4 wave plate. For each feature in the spectrum, β is determined from

$$\beta = \frac{I_{0^\circ} - I_{90^\circ}}{1/2 I_{0^\circ} + I_{90^\circ}}, \quad (3)$$

where I_{0° and I_{90° are the photoelectron intensities at $\theta = 0^\circ$ and $\theta = 90^\circ$.[25] In the absence of vibronic coupling and resonances in the photodetachment cross section the asymmetry parameter is not expected to change rapidly for transitions to a single electronic state but can vary for transitions to different electronic states.

III. RESULTS

A. Photoelectron spectra

The 355 and 266 nm photoelectron spectra of B_2N^- recorded at $\theta = 0^\circ$ and $\theta = 90^\circ$ are shown in Figs. 1 and 2. Spectra are shown as a function of eKE (top axis) and eBE (bottom axis), the later being more useful for comparison between detachment wavelengths as it is independent of the photon energy. Peaks observed in both spectra are better resolved in the 355 nm spectra, because the electron energy resolution deteriorates with increasing eKE. Positions, asymmetry parameters, and assignments for observed peaks,

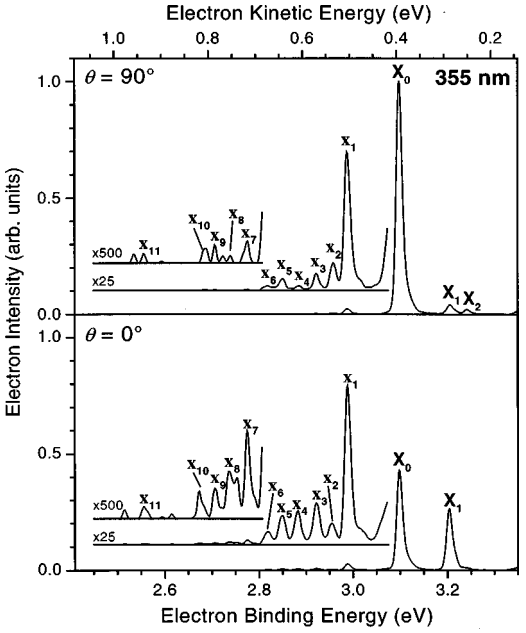

FIG. 1. 355 nm anion photoelectron spectra at $\theta = 90^\circ$ (top spectrum) and $\theta = 0^\circ$ (bottom spectrum) of B_2N^- plotted against electron binding energy (bottom axis) and electron kinetic energy (top axis). Selected parts of the spectra are also shown at vertical magnifications of ×25 and ×500. See Table I for peak positions, asymmetry parameters and peak assignments.

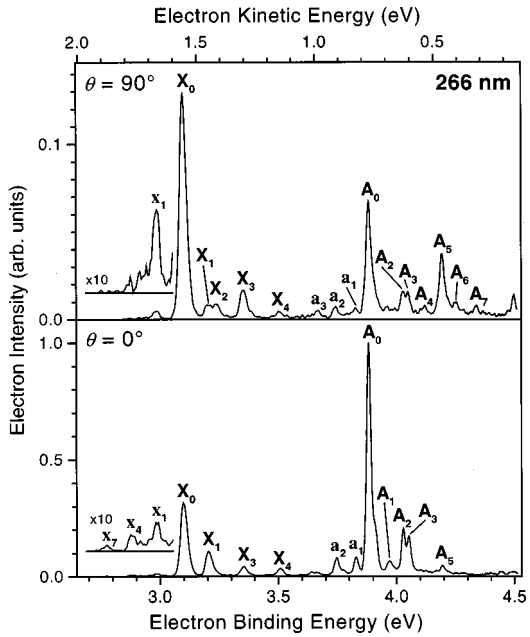

FIG. 2. 266 nm anion photoelectron spectra at $\theta = 90^\circ$ (top spectrum) and $\theta = 0^\circ$ (bottom spectrum) of B_2N^- plotted against electron binding energy (bottom axis) and electron kinetic energy (top axis). A selected region of both spectra is shown at a magnification of ×10. See Table I for peak positions, asymmetry parameters, and peak assignments.

TABLE I. Electron binding energies of peak maxima and asymmetry parameters (β) for the 355 and 266 nm photoelectron spectra of B_2N^- measured at $\theta=0°$ and $\theta=90°$. Simulated (Sim.) and averaged experimental (Expt.) peak positions and their difference ($\pm$) as well as peak assignments are also listed.

Peak	355 nm $\theta=90°$	355 nm $\theta=0°$	$\beta_{355\text{ nm}}$	266 nm $\theta=90°$	266 nm $\theta=0°$	$\beta_{266\text{ nm}}$	Expt.	Sim.[a]	$\pm$	Assignment
					$\tilde{X}\,^1\Sigma_g^+ \rightarrow \tilde{X}\,^2\Sigma_u^+ + e^-$					
x_{11}	2.556	2.557	+0.2				2.557	2.559	2	3_3^1
x_{10}	2.686	2.673	+0.5				2.679	2.679	0	1_3^0 (and 3_2^0)
x_9	2.706	2.707	+0.4				2.707	2.709	+2	$1_2^0 3_1^1$
x_8	2.739	2.737	+1.3				2.738	2.743	+5	$1_1^0 3_1^0$
x_7	2.775	2.775	+1.0		2.774	+1.9	2.775	2.774	−1	3_2^1
x_6	2.818	2.819	+0.7				2.818	2.818	0	1_2^0
x_5	2.850	2.849	+0.7				2.850	2.849	−1	$1_1^0 3_1^1$
x_4	2.885	2.882	+1.4		2.883	+1.4	2.884	2.883	−1	3_1^0
x_3	2.922	2.922	+0.7				2.922	2.922	0	3_2^2
x_2	2.958	2.955	−0.2				2.956	2.958	+2	1_1^0
x_1	2.988	2.988	+0.1	2.987	2.987	+0.7	2.988	2.989	+1	3_1^1
X_0	**3.098**	**3.098**	**−0.5**	**3.098**	**3.099**	**+0.7**	**3.098**	(**3.098**)		0_0^0
X_1	3.205	3.204	+1.3	3.204	3.204	+1.6	3.204	(3.204)		3_0^1
X_2	3.241		−0.4	3.239		+0.6	3.240	3.240	0	1_0^1
X_3				3.353	3.353	+0.7	3.353	(3.353)		3_0^2 (and $1_0^1 3_0^1$)
X_4				3.506	3.507	+1.4	3.506			3_0^3
					$\tilde{X}\,^1\Sigma_g^+ \rightarrow \tilde{A}\,^2\Sigma_g^+ + e^-$					
a_3				3.671		+0.7	3.671	3.668	−3	3_1^0
a_2				3.744	3.746	+1.5	3.745	3.744	−1	1_1^0
a_1				3.828	3.828	+1.6	3.828			3_0^5 ($\tilde{X}^2\Sigma_u^+$)
A_0				**3.884**	**3.883**	**+1.6**	**3.883**	(**3.883**)		0_0^0
A_1					3.970	+1.5	3.970	3.975	+5	3_1^1
A_2				4.030	4.028	+1.6	4.029	4.031	+2	1_0^1
A_3				4.049	4.051	+1.5	4.050			
A_4				4.121	4.123	+0.8	4.122	4.122	0	$1_0^1 3_1^1$
A_5				4.193	4.192	+0.2	4.193	4.190	−3	3_0^1
A_6				4.250		+0.3	4.250			
A_7				4.337		−0.2	4.337	4.337	0	$1_0^1 3_0^1$

[a]Values in parentheses indicate peak positions taken from experiment and were not optimized in the simulation. The positions of peaks X_1 and X_3 were used to determine the position of the corresponding hot bands.

which are labeled with either a capital or a small, indexed character, are listed in Table I. No additional transitions were observed at lower binding energies.

The spectra are dominated by two well-separated peaks, X_0 and A_0, which are assigned to the vibrational origin transitions to two electronic states of B_2N. Their asymmetry parameters are quite different at 266 nm (0.7 for X_0 and 1.6 for A_0), indicating electron photodetachment from two qualitatively different molecular orbitals (MOs). The asymmetry parameters of peak X_0 at 266 nm is more positive than at 355 nm, reflecting a rather strong dependence of β on eKE. Assuming X_0 corresponds to the transition between the anion and neutral ground states, its eBE yields the electron affinity of $B_2N(3.098\pm0.005\,\text{eV})$. A_0 then indicates the origin of an excited state of B_2N with term value $T_0=0.785\pm0.005\,\text{eV}$, the spacing between peaks X_0 and A_0. The dominance of both origin peaks is characteristic of vertical transitions with little change in the equilibrium geometry upon photodetachment.

Several smaller peaks with varying asymmetry parameters are also observed. Peaks X_1-X_4 are attributed to two vibrational progressions in the ground electronic state of B_2N. One progression includes peak X_2 and the shoulder on the higher energy side of peak X_3(eBE$\cong$3.39 eV) and is characterized by asymmetry parameters similar to the origin X_0. Since Franck–Condon (FC) allowed transitions to excited vibrational levels generally have the same asymmetry parameters as the vibronic origin, these peaks are assigned to the $v=1$ and $v=2$ levels of a totally symmetric vibrational mode with a fundamental frequency of $1143\pm40\,\text{cm}^{-1}$.

Peaks X_1, X_3, and X_4 are attributed to excitation of the $v=1-3$ levels of a second vibrational mode. The peak spacings $\Delta E_{ij}=E_j-E_i$ of this progression increase with the level of excitation ($\Delta E_{01}=855\,\text{cm}^{-1}$, $\Delta E_{12}=1197\,\text{cm}^{-1}$, $\Delta E_{23}=1239\,\text{cm}^{-1}$) and agree with the frequencies observed in the matrix IR spectrum.[12] While the asymmetry parameter for peak $X_2(v=2)$ is similar to that for the origin peak X_0, those for $X_1(v=1)$ and $X_4(v=3)$ are considerably more positive and in fact are close to β for peak A_0, the origin of the second electronic state. These large variations in β, depending on whether the upper state vibrational quantum is even or odd, suggest that this progression be assigned to a nontotally symmetric vibration. Within the FC approximation, the selection rule for nontotally symmetric modes is $\Delta v=0,\pm2,\pm4,...$, i.e., only even quanta transitions are allowed, in contrast to totally symmetric modes ($\Delta v=0,\pm1,\pm2,...$). The appearance of odd quanta transitions for nontotally symmetric modes thus points to a breakdown of the FC

approximation resulting, as discussed in Sec. V, from vibronic coupling to the excited state. Comparison to *ab initio* calculations (see below) indicates that the totally and nontotally symmetric modes are the symmetric and antisymmetric stretches, respectively, of linear B–N–B.

The region below X_0 in the 355 nm spectra shows a rich structure with at least 11 weak, irregularly spaced peaks (x_1–x_{11}) with widely varying β values. The intensity of these peaks depends strongly on the source conditions. We assign them to transitions originating from vibrationally excited levels of the anion (hot and sequence bands). The signal at lower *e*BE than peak X_0 is also observed in the 266 nm spectra but with less structure. Specific peak assignments based on simulated photoelectron spectra described in Sec. IV, are listed in Table I. These simulations yield fundamental frequencies for the anion ground state of $1130 \pm 40\ \mathrm{cm}^{-1}$ and $1728 \pm 40\ \mathrm{cm}^{-1}$, assigned to the symmetric and antisymmetric stretch, respectively, based on the comparison below with *ab initio* calculations.

The second electronic transition with origin A_0 is only observed in the 266 nm spectra. Based on the anion vibrational frequencies, we assign peaks a_2 and a_3 to vibrational hot bands. The assignment of the vibrational structure above the origin A_0 is complicated by the absence of any obvious vibrational patterns and varying asymmetry parameters. We postpone a more detailed discussion of this part of the photoelectron spectrum until after the description of the results of the electronic structure calculations, but note that the best agreement with the simulated photoelectron spectra is found by assuming activation of two vibrational modes: a totally and a nontotally symmetric mode with fundamental frequencies of $1174 \pm 40\ \mathrm{cm}^{-1}$ (A_0–A_2 spacing) and $2492 \pm 40\ \mathrm{cm}^{-1}$($A_0$–$A_5$), respectively.

B. Electronic structure calculations

Electronic structure calculations were carried out with the GAUSSIAN program packages.[26,27] Calculations with GAUSSIAN92 were performed on a Silicon Graphics Octane workstation at the University of California in Berkeley. GAUSSIAN94 calculations were performed on the Cray J90 SE cluster at the National Energy Research Scientific Computing Center at the Lawrence Berkeley National Laboratory.

The correlation consistent polarized valence basis sets of Dunning and co-workers, denoted by cc-pV*x*Z, where $x = \mathrm{D}$ (double zeta) and T (triple zeta), have been used in the present work.[28] Additional diffuse functions are especially important for the description of the electronic structure of molecular anions, and we therefore predominantly used the augmented correlation consistent sets of Kendall *et al.*,[29] denoted by aug-cc-pV*x*Z($x = \mathrm{D,T}$). Geometries and harmonic frequencies were determined using density functional theory (DFT) and coupled cluster theory. The DFT calculations were performed using the B3LYP (Becke-3-parameter-Lee–Yang–Parr) exchange-correlation functional.[30,31] For the coupled cluster calculations we used the CCSD(T) method,[32] where CCSD(T) stands for the coupled cluster with all single and double substitutions (CCSD)[33] augmented with a perturbative estimate of connected triple excitations. For all states presented here, the T_1 diagnostic, which is a rough measure of the importance of nondynamical correlation effects, was evaluated.[34] A sufficiently small T_1 value ($<\sim 0.02$) indicates that the CCSD(T) relative energies should be close to the full CI values.

In order to characterize the low-lying electronic states, we first scanned the configurational space at the computationally less demanding B3LYP/aug-cc-pVDZ level of theory. At selected stationary points harmonic frequencies were calculated analytically. For selected solutions, geometries and frequencies were then also determined employing the more flexible aug-cc-pVTZ basis set. The B3LYP model often predicts geometries and frequencies that are in reasonable agreement with experiment. Calculated adiabatic EAs are generally within ± 0.26 eV of the experimental value, although for notorious cases the deviation can be larger than 1 eV.[35,36] In order to get a more reliable estimate of the energetics of the B_2N^-/B_2N system, in particular the adiabatic detachment energies (ADEs), we also determined minimum-energy geometries and harmonic frequencies of selected states at the CCSD(T) level of theory using the aug-cc-pVDZ and aug-cc-pVTZ basis sets. Harmonic frequencies were determined by double numerical differentiation. It has been shown that calculations at the CCSD(T)/aug-cc-pVTZ level yield electron affinities for the GAUSSIAN-2 collection of atoms and molecules with an absolute error of $\leqslant \pm 0.15$ eV.[37]

1. Anion manifold

The stability of various isomers of B_2N^- has been studied previously at the QCISD(T)/6-31G* level of theory employing UHF/6-31G* optimized geometries.[38] The $^1\Sigma_g^+$ ground state of linear $(\mathrm{B–N–B})^-$ was found to be the absolute minimum. Linear B–B–N and cyclic B_2N anion structures were predicted to lie more than 1.9 eV above the $^1\Sigma_g^+$ ground state. Harmonic frequencies were determined at the UHF/6-31G* and MP2/6-31G* levels of theory. We have reinvestigated the anion manifold of B_2N^- at the B3LYP and CCSD(T) levels of theory. Results of the calculations, including the relative energies, equilibrium geometries, and force fields, were then used to simulate the photoelectron spectra. The present study confirms the previously predicted trends, but the higher level of theory employed here yields better agreement with experiment.

Calculated geometries, harmonic frequencies, and energies at the B3LYP/aug-cc-pVTZ and CCSD(T)/aug-cc-pVTZ levels of theory of electronic states considered in the present study are listed in Table II. The results of both theoretical models agree and unambiguously predict a closed-shell $^1\Sigma_g^+$ ground state with a linear, symmetric B–N–B arrangement ($D_{\infty h}$ symmetry). The valence orbital occupancy of this state is $(3\sigma_g)^2(2\sigma_u)^2(1\pi_u)^4(4\sigma_g)^2(3\sigma_u)^2$. The two highest occupied MOs are shown in Fig. 3. Both orbitals are predominantly nonbonding with the electron density localized mainly on the (terminal) boron atoms. Based on the energies in Table II, all photodetachment transitions observed in the present experiment should originate from the $\tilde{X}\,^1\Sigma_g^+$ state of linear B–N–B. At the CCSD(T)/aug-cc-pVTZ level of theory, the $\tilde{X}\,^1\Sigma_g^+$ state is characterized by a B–N bond length of 1.34 Å and harmonic frequencies of 1126 cm^{-1} (ω_1, symmetric stretching), 149 cm^{-1} (ω_2,

TABLE II. Calculated total energies (in a.u.), electronic term energies T_e and T_0 (in eV), bond lengths r (in Å), bond angles α (in °), harmonic frequencies ω (in cm^{-1}), spin $\langle S^2\rangle$, and T_1 diagnostic $\langle T_1\rangle$ for low-lying electronic states of B_2N^- at the B3LYP/aug-cc-pVTZ and CCSD(T)/aug-cc-pVTZ levels of theory.

Symmetry	State	Method	T_e	T_0	r_{BN}	r_{BB}	α_{BNB}	ω_1	ω_2	ω_3	$\langle S^2\rangle$	$\langle T_1\rangle$
$D_{\infty h}$ (BNB)[a]	$^1\Sigma_g^+$	B3LYP	0.000[d]	0.000	1.324			1156	179	1796	0.00	
		CCSD(T)	0.000[e]	0.000	1.337			1126	149	1756	0.00	0.015
	$^3\Pi_u$	B3LYP	2.637	2.639	1.327			1148	294[f]	1449	2.03	
		CCSD(T)	2.714	2.715	1.343			1111	272[f]	1537	2.38	0.072
$C_{\infty v}$ (BBN)[b]	$^1\Sigma^+$	B3LYP	2.439	2.423	1.273	1.635		795	196	1869	0.00	
		CCSD(T)	2.313	2.296	1.294	1.650		782	174	1767	0.00	0.030
C_{2v} (B_2N)[c]	$^3B_2$	B3LYP	2.124	2.123	1.386	1.629	72.0	1405	792	1095	2.02	
		CCSD(T)	2.136	2.136	1.405	1.648	71.8	1358	768	1064	2.06	0.034

[a] $\omega_{1\ldots3}=\sigma_g,\pi_u,\sigma_u$.
[b] $\omega_{1\ldots3}=\sigma_{(g)},\pi,\sigma_{(u)}$.
[c] $\omega_{1\ldots3}=a_1,a_1,b_2$.
[d] $E_{tot}=-104.468\,53$ a.u.
[e] $E_{tot}=-104.221\,84$ a.u.
[f] Mean harmonic frequency.

bending), and 1756 cm^{-1} (ω_3, antisymmetric stretching). The ω_1 and ω_3 frequencies are in excellent agreement with the experimental values ($1130\pm40\,cm^{-1}$ and $1728\pm40\,cm^{-1}$) determined by analysis of the hot bands.

The lowest excited triplet state in the $D_{\infty h}$ representation is predicted to be a $^3\Pi_u$ state, lying roughly 2.7 eV above the $\tilde{X}\,^1\Sigma_g^+$ state. Similar results for this state are obtained from both theoretical models. However, the unrestricted CCSD(T) wave function is considerably spin contaminated and characterized by a large T_1 value. A $^3\Sigma_g$ excited state, corresponding to the promotion of an electron from the highest occupied molecular orbital (HOMO), $3\sigma_u$, to the $4\sigma_u$ MO is predicted to be considerably above the $^3\Pi_u$ state.

The linear B–B–N arrangement ($C_{\infty v}$ symmetry) and the cyclic B_2N arrangement (C_{2v} symmetry) were also considered. The lowest energy structures for these arrangements are predicted to lie more than 2 eV above the B–N–B $\tilde{X}\,^1\Sigma_g^+$ state at all levels of theory considered here. The lowest energy solution for the B–B–N arrangement is a closed-shell $^1\Sigma^+$ state with bond distances of $r_{BN}=1.29$ Å and $r_{BB}=1.65$ Å. A $^3B_2$ state with a B–N–B bond angle (labeled as α_{BNB} in Table II) of 72° was found to be the absolute minimum for the cyclic configuration. HF/6-31+G*, B3LYP/aug-cc-pVDZ and CCSD(T)/aug-cc-pVDZ calculations for the lowest cyclic closed-shell species ($^1A_1$) indicated no minimum at a bent geometry, but rather converged to the linear B–N–B solution ($\tilde{X}\,^1\Sigma_g^+$).

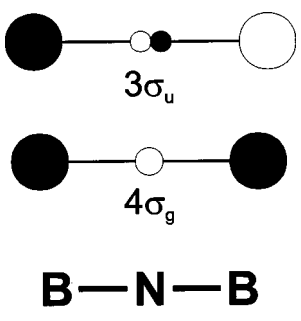

FIG. 3. Highest two occupied molecular orbitals of B_2N^-, calculated at the HF/6-31G level of theory and visualized using MOPLOT (Ref. 51).

2. Neutral manifold

Several *ab initio* studies have been performed on the neutral manifold of B_2N.[11,12,18,19,38] Knight *et al.*[11] found two minimum structures, linear B–N–B and cyclic B_2N. The global minimum at the UHF/6-31G* level is a cyclic $^2B_2$ state, while more highly correlated methods predict the $^2\Sigma_u$ state of linear B–N–B to be the global minimum and the cyclic $^2B_2$ state a local minimum. Martin *et al.*[18,38] tested the relative stability of a larger variety of structures up to the full fourth-order Møller–Plesset level of theory, determined harmonic frequencies, and estimated dissociation energies. They also found a linear $^2\Sigma_u$ ground state with harmonic frequencies at the MP2/6-31G* level of theory of 1100 cm^{-1}(ω_1), 142 cm^{-1}(ω_2), and 2225 cm^{-1}(ω_3). However, in a subsequent *ab initio* study on B_3N_2, Martin *et al.*[19] noted that the full valence CASSCF wave function for the $^2\Sigma_u$ state of linear B–N–B is unstable with respect to symmetry lowering, i.e., the $C_{\infty v}$ structure ($r_{BN}\neq r_{NB'}$) yields a lower total energy than the $D_{\infty h}$ structure ($r_{BN}=r_{NB'}$). To further investigate the symmetry breaking in B_2N and the relative stability of the cyclic isomer of B_2N, which has been invoked by Andrews *et al.*[12] in the interpretation of the matrix absorption spectrum of B_2N, we have performed B3LYP and coupled cluster calculations on the neutral manifold of B_2N.

Calculated geometries, harmonic frequencies, total and relative energies at the B3LYP/aug-cc-pVTZ, and CCSD(T)/aug-cc-pVTZ levels of theory of the electronic states considered in the present study are listed in Table III. B3LYP and CCSD(T) predict the lowest energy isomer of neutral B_2N to have a linear, symmetric B–N–B arrangement ($D_{\infty h}$). The ground state is the $^2\Sigma_u$ state with a valence orbital occupancy of $(3\sigma_g)^2(2\sigma_u)^2(1\pi_u)^4(4\sigma_g)^2(3\sigma_u)^1$. At the B3LYP/aug-cc-pVTZ level of theory, the EA without zero-point correction of (linear) B_2N is 3.054 eV. CCSD(T)/aug-cc-pVTZ calculations yield EA=3.139 eV. The lowest electronically excited state of linear B–N–B is predicted to be

TABLE III. Calculated total energies (in a.u.), electronic term energies T_e and T_0, adiabatic detachment energies ADE_e and ADE_0 (in eV), bond lengths r (in Å), bond angles α (in °), harmonic frequencies ω (in cm^{-1}), spin $\langle S^2\rangle$, and T_1 diagnostic $\langle T_1\rangle$ for low-lying electronic states of B_2N^- at the B3LYP/aug-cc-pVTZ and CCSD(T)/aug-cc-pVTZ levels of theory.

Symmetry	State	Method	T_e	T_0	ADE_e[h]	ADE_0[h]	r_{BN}	r_{BB}	α_{BNB}	ω_1	ω_2	ω_3	$\langle S^2\rangle$	$\langle T_1\rangle$
$D_{\infty h}$ (BNB)[a]	$^2\Sigma_u^+$	B3LYP	0.000[f]	0.000	3.054	3.020	1.312			1196	124	1327	0.76	-
		CCSD(T)	0.000[g]	0.000	3.139		1.328			1143	85	1320*i*	0.81	0.030
	$^2\Sigma_g^+$	B3LYP	0.589		3.643		1.298			1270	126	2324*i*	0.76	-
		CCSD(T)	0.697		3.836		1.314						0.80	0.032
$C_{\infty v}$ (BBN)[b]	$^2\Sigma^+$	B3LYP	2.362	2.378	2.976	2.975	1.283	1.542		912	165	1788	1.05	-
		CCSD(T)[d]	2.168		3.010		1.310	1.577					2.17	0.099
C_{2v} (B_2N)[c]	$^4B_2$	B3LYP	2.120	2.155	3.049	3.052	1.379	1.732	77.8	1408	732	1189	3.79	-
		CCSD(T)	1.943		2.947	2.952	1.395	1.738	77.0	1367	746	1158	3.79	0.026
$C_{\infty v}$ (BNB)[b]	$^2\Sigma^+$	CCSD(T)[e]	0.028		3.167		1.280 1.383[h]			1052	339	1683	0.79	0.032

[a] $\omega_{1\ldots3}=\sigma_g,\pi_u,\sigma_u$.
[b] $\omega_{1\ldots3}=\sigma_{(g)},\pi,\sigma_{(u)}$.
[c] $\omega_{1\ldots3}=a_1,a_1,b_2$.
[d] aug-cc-p-VDZ basis set.
[e] Frequencies calculated with aug-cc-pVDZ basis set.
[f] $E_{tot}=-104.356\ 32$ a.u.
[g] $E_{tot}=-104.106\ 48$ a.u.
[h] Adiabatic detachment energy relative to anion ground state of similar geometry.
[h] r_{NB}.

the $\tilde{A}\,^2\Sigma_g^+$ state, with a valence orbital occupancy of $(3\sigma_g)^2(2\sigma_u)^2(1\pi_u)^4(4\sigma_g)^1(3\sigma_u)^2$. Its term energy T_e is 0.697 eV at the CCSD(T)/aug-cc-pVTZ level of theory. These results are consistent with the experimental values of $EA=3.098\pm0.005$ eV and $T_0=0.785\pm0.005$ eV, given in the previous section.

The calculated changes in equilibrium bond length for the $\tilde{X}\,^1\Sigma_g^+\rightarrow\tilde{X}\,^2\Sigma_u^+ + e^-$ and $\tilde{X}\,^1\Sigma_g^+\rightarrow\tilde{A}\,^2\Sigma_g^+ + e^-$ transitions are $\Delta r_{BN}\approx -0.01$ Å and $\Delta r_{BN}\approx -0.02$ Å, respectively. These relatively small changes are in agreement with the absence of extended vibrational progressions in the experimental spectra and reflect the nonbonding character of the MOs, from which the electrons are ejected. Upon photodetachment the electrons are formally removed from the $3\sigma_u$ and $4\sigma_g$ MOs, respectively. The fundamentally different nodal properties of the $4\sigma_g$ and $3\sigma_u$ MOs account for the large difference in the asymmetry parameters of these two photodetachment transition origins. In particular, photodetachment from MOs with g symmetry results in a photoelectron angular distribution comprised of odd partial waves $(p,f,\ldots)$ while even partial waves $(s,d,\ldots)$ result from a MO with u symmetry.[25]

Results of calculations on two other possible isomers of B_2N, linear B–B–N and cyclic B_2N, are also listed in Table III. The B3LYP and CCSD(T) results agree well for both species. The CCSD(T)/aug-cc-pVDZ wave function for linear B–B–N is strongly spin contaminated and characterized by a large T_1 value. The lowest-lying electronic state for linear B–B–N is a $^2\Sigma^+$ state, calculated ~2.3 eV above the $\tilde{X}\,^2\Sigma_u^+$ state of linear B–N–B. The lowest stable cyclic state found at the B3LYP and CCSD(T) levels of theory is a $^4B_2$ state, which is calculated 1.9 eV above the $\tilde{X}\,^2\Sigma_u^+$ state of linear B–N–B. Our results support the previous findings of Martin *et al.*[18]

We also performed calculations on the cyclic $^2B_2$ state, the global minimum for neutral B_2N at the UHF level of theory. In Fig. 4 potential energy scans are plotted as a function of the B–N–B bond angle α_{BNB} at the B3LYP, UHF, CCSD, and CCSD(T) levels of theory. UHF/cc-pVDZ calculations predict a cyclic structure ($r_{BN}=1.33$ Å, $\alpha_{BNB}=83°$), which lies 0.36 eV below the $^2\Sigma_u^+$ solution. At the CCSD/cc-pVDZ level of theory the potential energy remains nearly unchanged between 180° and 140° and exhibits very shallow minimum ($\Delta E=-0.02$ eV) at $\alpha_{BNB}=95°$. No minima at $\alpha_{BNB}<180°$ are observed at either the B3LYP/cc-pVDZ or the CCSD(T)/cc-pVDZ level of theory. We conclude that the minimum for the $^2B_2$ state is an artifact of the UHF wave function and the lowest exact stable cyclic solution is the $^4B_2$ state. Note the similarities to B_2N^-, where the lowest stable bent solution is a $^3B_2$ state and not a singlet state.

Based on the calculated energetics and geometries, it appears that the B_2N^- photoelectron spectrum is comprised of transitions between linear B_2N^- and the ground and first excited states of linear B_2N, with all states having $D_{\infty h}$ symmetry. This assignment is further supported by comparison with the vibrational frequencies given below.

3. Vibrational frequencies

The B3LYP/aug-cc-pVTZ calculations yield harmonic vibrational frequencies of 1196 cm^{-1}(ω_1) and 124 cm^{-1}(ω_2) for the symmetric stretching and bending modes of the $\tilde{X}\,^2\Sigma_u^+$ ground state The CCSD(T)/aug-cc-pVTZ results are similar, yielding 1143 cm^{-1}(ω_1) and 85 cm^{-1}(ω_2). Compared to the anion ground state, the symmetric stretch frequency remains essentially unchanged, while the already low anion bending frequency is even lower in the neutral, indicating an extremely floppy B–N–B molecule. For the $\tilde{A}\,^2\Sigma_g^+$ state, calculations at the B3LYP/aug-cc-pVTZ level predict harmonic frequencies of 1270 cm^{-1}(ω_1) and 126 cm^{-1}(ω_2). Previous calculations at the UHF/6-31G* level (scaled) yielded 1203 cm^{-1}(ω_1) and 392 cm^{-1}(ω_2).[12] As discussed in Sec. III A, the photoelectron spectra indicate there are totally symmetric vibrations of the $\tilde{X}$ and $\tilde{A}$ states with fre-

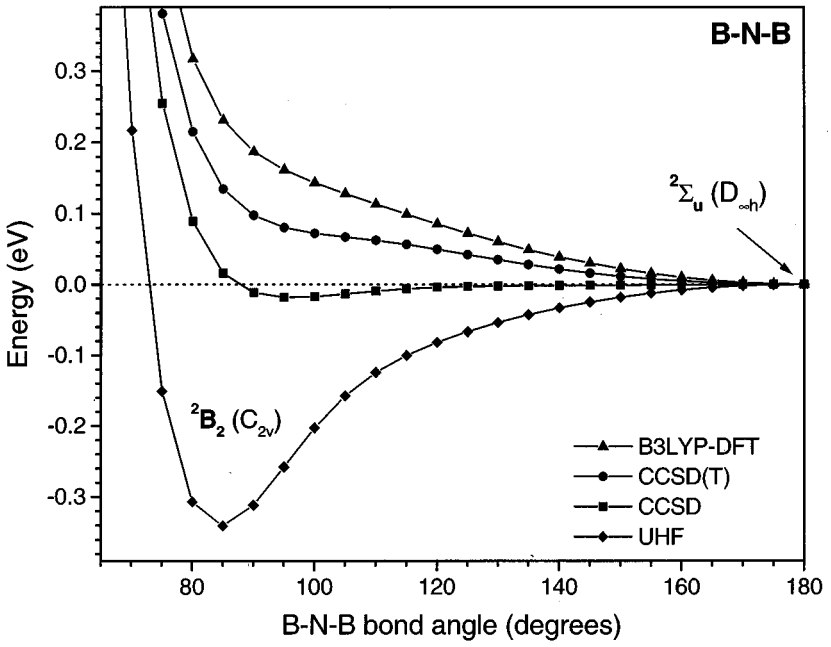

FIG. 4. Potential energy as a function of B–N–B bond angle α_{BNB} of the ground state of B_2N calculated at the B3LYP, UHF, CCSD, and CCSD(T) levels of theory employing the cc-pVDZ basis set. The potential energy at the optimized $D_{\infty h}$ geometry ($\alpha_{BNB}=180°$) is chosen as the origin of the energy scale. Lines connecting symbols are shown to aid the eye.

quencies 1143 ± 40 and $1174\pm40\,cm^{-1}$, respectively; these agree with the calculated symmetric stretch frequencies.

The nontotally symmetric progression in the lower energy band, in which the first two peaks are separated by 855 cm^{-1}, must therefore correspond to the antisymmetric (ν_3) stretch of the neutral ground state. However, complications were encountered in the determination of this frequency. Calculations at the B3LYP/aug-cc-pVTZ level predict a harmonic frequency for the ν_3 mode of 1327 cm^{-1}. The scaled UHF/6-31G* and MP-2/6-31G* harmonic frequencies (2021 and 2225 cm^{-1}, respectively)[18,38] are considerably higher. None of these results are in satisfactory agreement with the experiment. Attempts to determine the harmonic frequency at the CCSD(T) level of theory failed. Characterization of the ν_3 mode of the $\tilde{A}$ state is even more problematic, because distortion along the antisymmetric stretch coordinate yields a wave function which is not the lowest energy solution with $^2\Sigma^+$ symmetry.

Closer inspection of the ν_3 potential of the $\tilde{X}\,^2\Sigma_u^+$ ground state reveals the reasons for the complications encountered in the determination of its harmonic frequency and the disagreement with the experimental results. Figure 5 shows the results of potential energy scans along the antisymmetric stretch normal coordinate Q_3, calculated at the B 3 LYP/cc-pVDZ and CCSD(T)/cc-pVDZ levels of theory. The UHF and CCSD potentials from the CCSD(T) calculations are also shown. Q_3 is given by

$$Q_3=\sqrt{\frac{2m_Bm_N}{2m_B+m_N}}\cdot\frac{r_{BN}-r_{NB'}}{2}$$

$$\text{with}\quad r_{BB'}\equiv r_{BN}+r_{NB'}=\text{const.} \tag{4}$$

Here m_B and m_N are the masses of atomic boron and nitrogen, respectively, and r_{BN}, $r_{NB'}$ and $r_{BB'}$ are the internuclear distances. The origin of the energy scale was chosen arbitrarily to coincide with the energy at the optimized $D_{\infty h}$ geometry ($r_{BN}=r_{NB'}$). The CCSD(T) calculations converged to two qualitatively different solutions, depending on the starting orbitals used. Potentials corresponding to the lowest eigenvalue at the UHF and CCSD levels of theory are indicated by the solid lines in Fig. 5. The broken lines correspond to the potentials of the second solution.

The B3LYP ν_3 potential is nearly harmonic, exhibiting a single well with a minimum at the $D_{\infty h}$ structure. On the other hand, an instability in the lowest UHF wave function is found around this geometry. The UHF potential displays a double well character, with minima at the $C_{\infty v}$ arrangements.

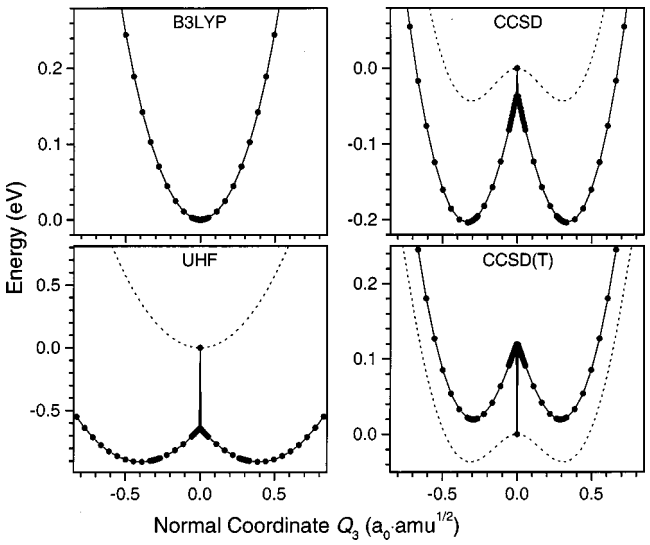

FIG. 5. Potential energy (solid circles) along the antisymmetric stretch coordinate Q_3 [see Eq. (4)] for the ground state of linear B–N–B calculated at the B3LYP, UHF, CCSD, and CCSD(T) levels of theory employing the cc-pVDZ basis set. The potential energy at the $D_{\infty h}$ geometry ($Q_3=0$) is chosen as the origin for each energy scale. Solid lines are shown to aid the eye. Broken lines indicate a second solution to which the calculations converge to (see text).

It is discontinuous, displaying a cusp around the $D_{\infty h}$ geometry ($Q_3=0$, $r_{BN}=r_{NB'}$), where the energy is more than 0.6 eV higher than at a slightly distorted geometry, e.g., $r_{BN}-r_{NB'}=2\times10^{-4}$ Å ($Q_3=6\times10^{-4}$ Bohr amu$^{1/2}$). This instability propagates to the CCSD and CCSD(T) solutions. The overall form of the potential at the CCSD level is qualitatively similar to the UHF potential, although the increase in energy at the $D_{\infty h}$ solution is more than an order of magnitude smaller. At the CCSD(T) level the situation changes. Although the discontinuity at the $D_{\infty h}$ geometry remains, the energy does not increase but it decreases by roughly 0.15 eV with respect to the slightly distorted solution. Moreover, the $D_{\infty h}$ solution at the CCSD(T) level lies 0.02 eV *below* the $C_{\infty v}$ minima.

The broken lines shown for the UHF, CCSD, and CCSD(T) models in Fig. 5 indicate a second solution, to which the calculations converged to for $|Q_3|<0.78$ Bohr amu$^{1/2}$. Convergence to this solution was achieved by optimizing the MOs at a minimally distorted $D_{\infty h}$ geometry, e.g., $Q_3=6\times10^{-4}$ Bohr amu$^{1/2}$, and then using these MOs for any subsequent calculations at larger values of Q_3. This solution does not represent the lowest eigenvalue at both the UHF and CCSD levels of theory away from the $D_{\infty h}$ symmetry. It does result in a lower energy for the CCSD(T) model. At all three levels of theory this second solution yields potentials, which do not suffer from any discontinuities. The UHF potential is a single well, while both the CCSD and CCSD(T) potentials are double well potentials.

The solution corresponding to the lowest UHF eigenvalue is clearly nonphysical, because it is discontinuous in all three cases. The quality of the second solution is, however, also questionable, as it is based on wave functions which do not represent the lowest energy solution within the given irreducible symmetry representation. This also holds for the CCSD(T) calculations, because the perturbative estimate of the connected triple excitations is derived from the optimized CCSD wave function. Inspection of Fig. 5 clearly demonstrates three points: (1) determination of an antisymmetric stretch *harmonic* frequency using the UHF, CCSD, and CCSD(T) models does not yield a physically meaningful solution, (2) the contribution of higher than doubly excited configurations to the CCSD(T) energy is important, indicating a strong multiconfigurational character of the exact wave function, and (3) the UHF, CCSD, and CCSD(T) wave functions for the ground state of B–N–B based on the lowest UHF solution indicate that symmetry breaking effects are important.

4. Symmetry breaking

The discontinuous potential energy functions in Fig. 5 are a likely signature of *artifactual* symmetry breaking, i.e., the form assumed for the approximate wave function is oversimplified and leads to artifactual structure on the potential energy surface.[39] Furthermore, the wave function will change discontinuously as the molecule is distorted along the symmetry breaking coordinate. If the approximate wave function attains a lower energy by breaking the spatial symmetry present in the exact wave function we speak of the

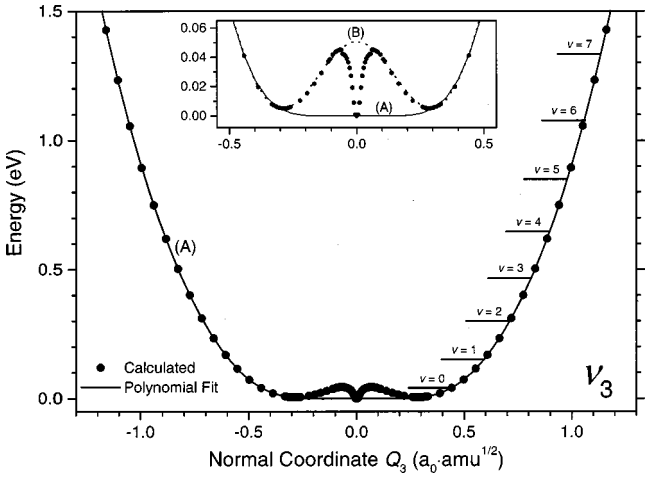

FIG. 6. Potential energy (solid circles) along the antisymmetric stretch coordinate Q_3 [see Eq. (4)] of the $\tilde{X}\,^2\Sigma_u^+$ state of B_2N calculated at the BD(T)/cc-pVDZ level of theory. This potential was fit to two polynomial functions (potential A and B, see text), which are represented by the solid line (A) and the broken line (B, only shown in the inset). The calculated eigenvalues of potential A for $v=0$ to $v=7$ are indicated by the horizontal lines.

''symmetry dilemma.'' [40] Prediction of the symmetry of the exact wave function based on approximate wave functions exhibiting artifactual symmetry breaking is generally not possible.

A standard approach to symmetry breaking problems is the use of multiconfigurational wave functions, which allow for the proper mixing of competing, near-degenerate valence bond structures.[41–43] Alternative methods include coupled cluster theory using Brueckner orbitals and DFT methods.[43–45] The B3LYP results show no sign of symmetry breaking, but fail to reproduce the experimental vibrational frequency. Therefore, we chose to perform CCSD(T) calculations employing Brueckner orbitals, abbreviated BD(T),[44,46] to characterize the antisymmetric stretch potential $V(Q_3)$. The BD(T) potential curve is shown in Fig. 6. Although the instability around the $D_{\infty h}$ arrangement remains, it is less evident that in the CCSD(T) calculations using the canonical orbitals, so the BD(T) potential curve represents a substantial improvement.

The extent of the symmetry breaking artifact in the BD(T) wave function is rather small. The observed increase in energy is 45 meV around the $D_{\infty h}$ structure, roughly the same magnitude as the expected zero-point energy of the ν_3 mode. To test if the BD(T) calculations nonetheless describe the ν_3 potential correctly away from $D_{\infty h}$ structure we determined vibrational eigenvalues. To this end, we fit two polynomial functions $V(Q_3)$ given by Eq. (5) to modified forms of the calculated BD(T) potential.

$$V(Q_3)=C_0+C_2Q_3^2+C_4Q_3^4+\cdots+c_{20}Q_3^{20}. \tag{5}$$

Here C_i are the expansion coefficients and Q_3 the normal coordinate of the antisymmetric stretch mode ν_3. As the dip in the potential for $Q_3=0$ is a result of the instability, we chose to fit two physically reasonable functions to the calculated potential. These functions, labeled (A) and (B), are shown in Fig. 6. The numerically determined eigenvalues for both functions are listed in Table IV.

TABLE IV. Calculated and experimentally determined eigenvalue spacings $\Delta E(\nu)-\Delta E(0)$ (in cm^{-1}) for the antisymmetric stretch mode ν_3 of the ground and first excited states of B_2N. ν is the vibrational quantum number. Numbers in parentheses refer to the zero point energy. Theoretical values are based on BD/cc-pVDZ potential energies (potentials A and B) and a linear vibronic coupling (LVC) model [Eq. (7)].

	Theory				Experiment	
	BD/cc-pVDZ		LVCmodel			PES[d]
ν	Potential A	Potential B	Uncoupled[a]	Coupled[b]	IR matrix [c]	($\pm$40 cm^{-1})
			$\tilde{X}\,^2\Sigma_u^+$			
0	0(332)	0(497)	0(864)	0(355)		
1	885	752	1728	902	882.3	855
2	2085	2016	3456	2053		2052
3	3431	3317	5184	3271	3330	3291
4	4897	4789	6912	4548		
5	6524	6416	8640	5864	5882	5888
6	8354	8246	10368	7212		
			$\tilde{A}\,^2\Sigma_g^+$			
0			0(864)	0(1177)		
1			1728	2365		2492
2			3456	4627		
3			5184	6829		

[a]$\lambda^2=0$.
[b]$\lambda^2=4.06\times10^{28}$ eV/s^2.
[c]Reference 12.
[d]Present work.

Function (A) was fit to the BD(T) potential ignoring all calculated points inbetween the $D_{\infty h}$ and $C_{\infty v}$ minima, but including the point at $Q_3=0$. As a result we attained a flat, single well potential. Note the first nonzero coefficient for function (A) is C_4, indicating that the potential is more quartic than harmonic in nature. For function (B) we retained the double well character of the potential by ignoring the dip around $Q_3=0$. The eigenvalues E_i determined for both of the potentials are similar. In particular the eigenvalue spacing $\Delta E_{ij}=E_j-E_i$ is rather insensitive to the exact form of the potential around $Q_3=0$ for these two functions, because the barrier height is smaller than the $\nu=0$ level in both cases. The agreement with the experiment is very good (see Table IV). Both functions quantitatively reproduce the observed eigenvalue spacing correctly including the negative anharmonicity. Note that the $\nu=1$ level ($\Delta E_{01}^A=752\,cm^{-1}$, $\Delta E_{01}^B=885\,cm^{-1}$) is unusually low compared, for example, to the ''unperturbed'' ν_3 fundamental of the anion ground state (1728 cm^{-1}).

IV. ANALYSIS

We can now simulate the experimental spectra within the FC approximation, assuming they are comprised of transitions from the $\tilde{X}\,^1\Sigma_g^+$ state of linear BNB^- to the $\tilde{X}\,^2\Sigma_u^+$ and $\tilde{A}\,^2\Sigma_g^+$ states of linear BNB. Two vibrational modes (ν_1 and ν_3) were included in the simulation. Harmonic potentials were employed, except for the ν_3 mode of the $\tilde{X}\,^2\Sigma_u^+$ state, where we used the previously discussed polynomial function (A) based on the BD(T)/cc-pVDZ potential energy curve. A harmonic potential for the ν_3 mode of the $\tilde{A}\,^2\Sigma_g^+$ state was constructed to match the spacing between peaks A_0 and A_5. For all other harmonic potentials the frequency and normal coordinate displacements were determined from the results of the B3LYP/aug-cc-pVTZ calculations. The harmonic frequencies of all harmonic modes and the normal coordinate displacements in the ν_1 modes were then optimized until the best agreement between the experiment and the simulation was achieved. Except for the relative overall intensity of the two electronic transitions and the mean vibrational temperature ($T_{vib}^{355\,nm}=800\,K$, $T_{vib}^{266\,nm}=1100\,K$), identical parameters were used to fit all four experimental spectra (355 and 266 nm spectra measured at two laser polarizations). Progressions in the ν_3 mode were simulated assuming $\Delta Q_3=0$ for FC-allowed (even $\Delta\nu_3$) transitions, while intensities of the FC forbidden transitions (which normally would be zero within the FC approximation) were scaled to the corresponding peaks in the experimental spectra to show where these transitions occur. The stick spectra generated in the simulation are convoluted with the experimental resolution function.

Figures 7 and 8 compare optimized simulations with experimental results for the $\theta=0°$ and $\theta=90°$ 266 nm photoelectron spectra of B_2N^-. FC allowed transitions are shaded black. Parameters used to generate the optimized simulations are listed in Table V and compared to those obtained directly from the DFT calculations; only minor changes in the symmetric stretch frequencies and normal coordinate displacements are required. Based on these simulations we can give an almost complete assignment of the features observed in the photoelectron spectra of B_2N^-; this is listed in Table I. We assign 16 peaks to the $\tilde{X}\,^1\Sigma_g^+\rightarrow\tilde{X}\,^2\Sigma_u^++e^-$ transition and eight peaks to the $\tilde{X}\,^1\Sigma_g^+\rightarrow\tilde{A}\,^2\Sigma_g^++e^-$ transition. All simulated peak positions lie within ±5 meV of the experimental value. Considering the experimental resolution, the elevated ion vibrational temperature and rotational contribu-

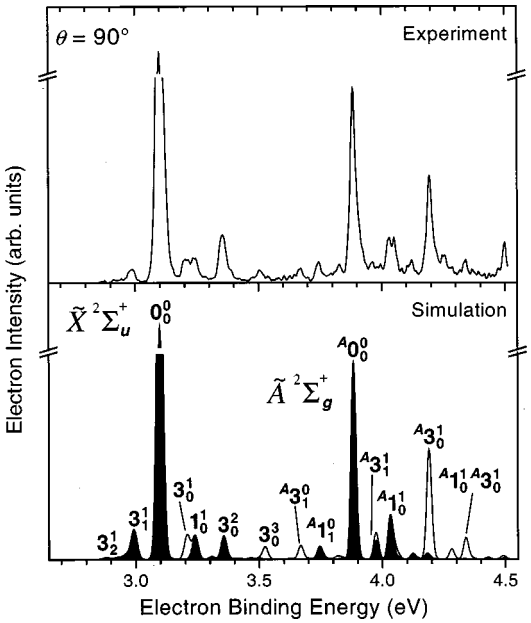

FIG. 7. Experimental $\theta=90°$, 266 nm photoelectron spectra of B_2N^- (top) and simulated $\theta=90°$, 266 nm spectrum (bottom). Black-shaded peaks indicate FC allowed transitions.

tions to the line shape, we estimate absolute errors for the electron affinity and for the properties derived from peak spacings to be not larger than ± 5 meV (± 40 cm^{-1}).

Peaks $X_2(1_0^1)$, $X_3(3_0^2)$, $x_1(3_1^1)$, $x_2(1_1^0)$, $x_3(3_2^2)$, $x_5(1_1^0 3_1^1)$, $x_6(1_2^0)$, $x_9(1_2^0 3_1^1)$, $x_{10}(1_3^0)$, and $x_{11}(3_3^1)$, are assigned to FC allowed $\tilde{X}\,^1\Sigma_g^+ \rightarrow \tilde{X}\,^2\Sigma_u^+ + e^-$ transitions. These transitions involve either excitation in the ν_1 mode only, excitation of even quanta in the ν_3 mode, or combinations of these two types of excitation. Peaks $X_1(3_0^1)$, $X_4(3_0^3)$, $x_4(3_1^0)$, $x_7(3_2^1)$, and $x_8(1_1^0 3_1^0)$ are assigned to FC forbidden transitions. They involve excitation of uneven quanta in the ν_3 mode. This assignment is supported by the peak asymmetry parameters. The asymmetry parameters of the FC forbidden transitions $(+1.4 \leqslant \beta_{266\text{ nm}} \leqslant +1.9, +1.0 \leqslant \beta_{355\text{ nm}} \leqslant +1.4)$ are all larger than those of the FC allowed transitions $(+0.6 \leqslant \beta_{266\text{ nm}} \leqslant +0.7, -0.4 \leqslant \beta_{355\text{ nm}} \leqslant +0.7)$. The larger scatter in the 355 nm asymmetry parameters is due in part to the pronounced eKE dependence of β at these energies indicated, for example, by the strong change in β from -0.5 at 355 nm to $+0.7$ at 266 nm for the origin peak X_0. In any case, the FC forbidden $\tilde{X}\,^1\Sigma_g^+ \rightarrow \tilde{X}\,^2\Sigma_u^+ + e^-$ transitions have asymmetry parameters similar to that of the excited state origin $A_0(\beta_{266}=+1.6)$, while the asymmetry parameters of the FC allowed transitions associated with this band are close to that of the ground state origin X_0.

Assignments of the peaks comprising the $\tilde{X}\,^1\Sigma_g^+ \rightarrow \tilde{A}\,^2\Sigma_g^+ + e^-$ transition are complicated by our lack of quantitative information on the ν_3 potential of the $\tilde{A}\,^2\Sigma_g^+$. Best agreement with the experimental data is achieved by assuming mean vibrational frequencies of 1172 cm^{-1} (ν_1) and 2467 cm^{-1} (ν_3). Excitation in only the ν_1 modes of the anion or the neutral results in the peaks $A_2(1_0^1)$ and $a_2(1_1^0)$. Excitation involving the ν_3 modes then accounts for the peaks at $a_3(3_1^0)$, $A_1(3_1^1)$, $A_4(1_0^1 3_1^1)$, $A_5(3_0^1)$, and $A_7(1_0^1 3_0^1)$. The 1_1^0, 1_0^1, and 3_1^1 transitions are allowed and show the same angular dependence as the origin peak A_0. The asymmetry parameter of the allowed $1_1^0 3_1^1$ transition is less positive than expected, but this weaker peak also lies in a rather congested part of the spectrum, making the determination of its asymmetry parameter less accurate. The asymmetry parameters of the observed ''forbidden'' vibronic transitions are close to the asymmetry parameters of the ground state origin X_0. The simulation does not account for peaks a_1, A_3, and A_6. Note that the spacing between peaks a_1 and X_0 is 5888 cm^{-1}, close to the intense signal observed at 5882 cm^{-1} in the matrix IR spectrum.[12] This indicates that peak a_1 is not a vibrational hot band of the $\tilde{A}$ state, and instead is due to a highly excited vibrational level of the $\tilde{X}$ state. Its intensity arises from vibronic coupling to the $\tilde{A}$ state, which we discuss in Sec. V.

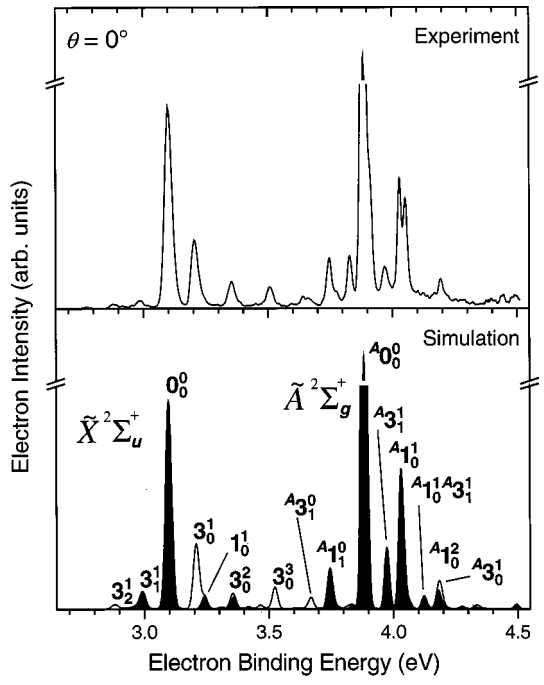

FIG. 8. Experimental $\theta=0°$, 266 nm photoelectron spectra of B_2N^- (top) and simulated $\theta=0°$, 266 nm spectrum (bottom). Black-shaded peaks indicate FC allowed transitions.

V. DISCUSSION

Observation of excitation of uneven quanta in a nontotally symmetric vibration clearly indicates a breakdown of the FC approximation. In the present case it is caused by the coupling of two nondegenerate states of different spatial symmetry via a single nontotally symmetric mode. This type of vibronic coupling is called Herzberg–Teller coupling[47] and results in a normal coordinate dependence of the electronic transition dipole moment. FC forbidden transitions may then be observed in the anion photoelectron spectrum, due to intensity borrowing from a FC allowed transition of identical vibronic symmetry. The asymmetry parameter of

TABLE V. Calculated (B3LYP) and optimized (opt.) parameters used for simulations of the photoelectron spectra of B_2N^-. Adiabatic detachment energies ADE_0 (in eV), harmonic frequencies ω (in cm^{-1}), and changes in symmetric stretch normal coordinate ΔQ_1 (in percent relative to Q_1 of the anion) are listed.

Transition	Method	ADE_0	Mode	ω^{anion}	$\omega^{neutral}$	ΔQ_1
$\tilde{X}\,^1\Sigma_g^+ \rightarrow \tilde{X}\,^2\Sigma_u^+ + e^-$	B3LYP	3.020	ν_1	1156	1196	6%
			ν_3	1796	1327	[c]
	opt.	3.098	ν_1	1128	1143	5%
			ν_3	1735	885/2085/3431[b]	[c]
$\tilde{X}\,^1\Sigma_g^+ \rightarrow \tilde{A}\,^2\Sigma_g^+ + e^-$	B3LYP	3.643[a]	ν_1	1156	1270	12%
			ν_3	1796		[c]
	opt.	3.883	ν_1	1128	1187	11%
			ν_3	1735	2471	[c]

[a] ADE_e.
[b] Eigenvalue spacings ΔE_{01}, ΔE_{02}, ΔE_{03} based on BD(T)/cc-pVDZ potential. Not optimized.
[c] FC forbidden ($\Delta Q_3 \equiv 0$). Intensities of FC forbidden transitions in Figs. 7 and 8 were scaled to experiment.

the peak corresponding to the forbidden transition is (in principle) determined by the spatial symmetry of the electronic state, from which it borrows its intensity.

The photoelectron spectrum of C_2H^- by Ervin and Lineberger[48] represents a nice example in which vibrational bands within a single electron transition showed markedly different photoelectron angular distributions. Here, non-FC behavior due to vibronic coupling between the $\tilde{X}\,^2\Sigma^+$ ground state and the $\tilde{A}\,^2\Pi$ first excited state of linear C–C–H manifested itself in the observation of transitions to the neutral ground state with odd changes in the vibrational quantum number of the nontotally symmetric C–C–H bend. These transitions are FC forbidden and the corresponding angular distributions are strikingly different from the FC allowed transitions. Taylor *et al.*[49] showed that these FC forbidden transitions are characterized by asymmetry parameters which reflect the angular distribution of the FC allowed transitions to the $\tilde{A}\,^2\Pi$ state, i.e., the state to which they are vibronically coupled.

The spectra of B_2N^- exhibit similar features. The vibronic symmetry of odd ν_3 levels in the $\tilde{X}\,^2\Sigma_u^+$ and $\tilde{A}\,^2\Sigma_g^+$ states is $\Sigma_u^+ \otimes \sigma_u^+ = \Sigma_g^+$ and $\Sigma_g^+ \otimes \sigma_u^+ = \Sigma_u^+$, respectively. The vibronic symmetry of the odd levels in one state is equal to the electronic symmetry of the other state and therefore the two states are coupled along the antisymmetric stretching coordinate. This vibronic coupling between the $\tilde{X}$ and $\tilde{A}$ states manifests itself in the observation of FC forbidden transitions involving the ν_3 modes. Measurement of the photoelectron angular distributions represents a sensitive tool for the identification of these FC forbidden transitions and also indicates the state to which they are coupled. However, the present case is different from vibronic coupling in C_2H^-, as it involves vibronic coupling between two electronic states of a linear molecule without involvement of the bending motion. This appears to be the first such observation in a photoelectron spectrum.

Vibronic coupling between the $\tilde{X}\,^2\Sigma_u^+$ ground state and the $\tilde{A}\,^2\Sigma_g^+$ lowest excited state of linear B–N–B is similar to the coupling predicted for weakly bound linear He_4^+ ion clusters by Tarantelli *et al.*[50] In both systems a Σ_u and a Σ_g state of a linear symmetric $D_{\infty h}$ system are coupled along the antisymmetric stretching mode Q_u (Q_3 in the present case). As the system is distorted along Q_u, the symmetry of the system is lowered to $C_{\infty v}$, the g/u symmetry is lifted, and the two states couple. If the coupling is strong enough, the interaction will lead to real (versus artifactual) symmetry breaking in the lower state. The interaction in the vicinity of $Q_u = 0$ can be modeled by the following Hamiltonian:[50]

$$\begin{bmatrix} 2\pi^2\nu^2 Q_u^2 & \lambda Q_u \\ \lambda Q_u & \Delta + 2\pi^2\tilde{\nu}^2 Q_u^2 \end{bmatrix}, \tag{6}$$

where Δ is the (positive) separation between the states at $Q_u = 0$, ν and $\tilde{\nu}$ are the harmonic frequencies (of the uncoupled system), and λ is the linear coupling coefficient.

Assuming $\nu = \tilde{\nu}$, the energies of the lower and upper potentials (V_1 and V_2) are given by

$$V_{1,2} = \tfrac{1}{2}(4\pi^2\nu^2 Q_u^2 + \Delta \mp \sqrt{4\lambda^2 Q_u^2 + \Delta^2}). \tag{7}$$

Symmetry breaking occurs if

$$\lambda^2 > 2\pi^2\nu^2\Delta. \tag{8}$$

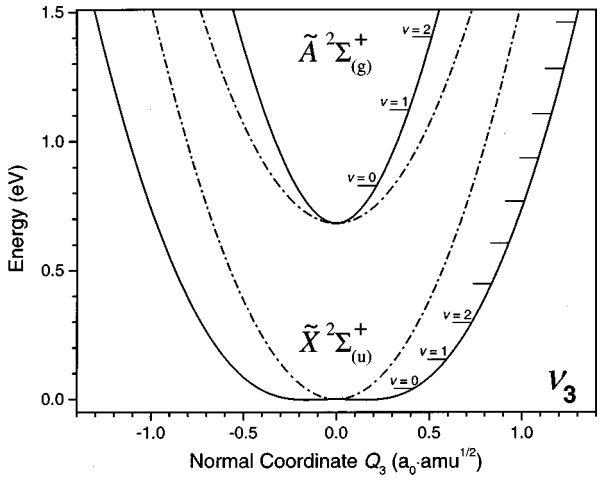

FIG. 9. Potential energy (solid lines) along the antisymmetric stretch coordinate Q_3 [see Eq. (4)] of the $\tilde{X}\,^2\Sigma_u^+$ and $\tilde{A}\,^2\Sigma_g^+$ state of B_2N assuming linear vibronic coupling (see text). Broken lines indicate uncoupled harmonic potentials. The calculated eigenvalues of both potentials are indicated by the horizontal lines.

In this case the potential energy along Q_u of the true state will be characterized by three stationary points, a maximum at $Q_u=0$ and two minima, appearing symmetric with respect to $Q_u=0$.[50] The vibrational frequency of the upper state will increase, due to destabilization of the upper potential (and the stabilization of the lower potential).

In Fig. 9 the uncoupled (broken lines) and linearly coupled ν_3 potentials (solid lines) for the $\tilde{X}\,^2\Sigma_u^+$ and $\tilde{A}\,^2\Sigma_g^+$ states of B_2N are shown using the linear vibronic coupling model described in the previous paragraph. As we have no direct measure for the (unperturbed) harmonic frequencies of both states, both are assumed to be equal to the fundamental frequency of the ν_3 mode in the anion ground state (1728 cm^{-1}). The separation between the two states $\Delta=0.683\,eV(\equiv T_e)$ was derived from the term energy of the $\tilde{A}\,^2\Sigma_g^+$ state ($T_0=0.785\,eV$) and the calculated zero point energies of the two states for a given value of λ. We then determined λ^2 by least square fitting of the three lowest eigenvalue spacings of the ν_3 mode in the $\tilde{X}\,^2\Sigma_u^+$ state to the values determined from the experiment, finding $\lambda^2=4.06\times10^{28}\,eV/s^2$. The eigenvalues of the two optimized potentials are listed in Table IV. The eigenvalue spacings for both the lower and upper potentials are in qualitative agreement with the experimental observations. Specifically, this simple model accounts for the low fundamental frequency and negative anharmonicity of the ν_3 mode in the ground state, as well as the high fundamental frequency in the electronically excited state. We also find that the $v=5$ level supported by the lower potential at 5864 cm^{-1} lies very close to the spacing between peaks X_0 and a_1 in the photoelectron spectrum (5888 cm^{-1}), suggesting that the latter peak be assigned as the $3_0^5(\tilde{X}\,^2\Sigma_u^+)$ transition.

Note that our value of λ^2 is slightly larger than $2\pi^2\nu^2\Delta(=3.62\times10^{28}\,eV/s^2)$, so that according to Eq. (8) real symmetry breaking should occur in the lower state. However, the barrier between the two $C_{\infty v}$ minima is only 18 cm^{-1}, more than an order of magnitude smaller than the zero point energy of 355 cm^{-1} for the lower potential (see Table IV).

The combination of the present experimental and theoretical data suggest that the ground state of linear B–N–B is an intermediate case of symmetry breaking. As a result the adiabatic potential of the ν_3 mode may be symmetry broken, but the zero point energy of the ν_3 mode is larger than the symmetry breaking barrier. In such a case the ground state of B–N–B would be *quasisymmetric* with respect to inversion. No conclusions can be made with respect to the quasisymmetric versus symmetric nature of the ground state on the basis of the present *ab initio* calculations, as these results are plagued by artifactual symmetry breaking. On the other hand, the B3LYP model clearly underestimates the extent of Herzberg–Teller vibronic coupling.

A. Matrix absorption spectrum

The present data allow us to suggest a revised interpretation of the matrix absorption spectrum of Andrews *et al.*[12] and resolve the discrepancy concerning the stability of the linear and bent isomers of B_2N. The assignment of the absorption spectrum was based on the following reasoning: (1) a potential energy surface search at the HF/6-31G* level of theory reveals a stationary point on the doublet surface which corresponds to a cyclic $^2B_2$ state; (2) the B_2N species observed in the absorption experiment is nonlinear B–N–B because the strong 882.3 cm^{-1} fundamental is too low; and (3) the isotopic shifts are inappropriate for linear B–N–B.

TABLE VI. Isotopic absorptions (cm^{-1}), absorbances (in parentheses), absorption ratios, and revised assignment for matrix absorption spectrum based on present PES data.

Absorption (matrix)			PES (gas phase)	Revised assignment
$^{11}B^{14}N^{11}B$	$^{11}B^{15}N^{11}B$	Ratio	$^{11}B^{14}N^{11}B$	
882.3 (.40)	862.3	1.023	855±40	$\Delta\nu_3=1$ ($\tilde{X}\,^2\Sigma_u^+$)
1736.5	1701.6	1.021	1728±40	$\Delta\nu_3=1$ ($\tilde{X}\,^1\Sigma_g^+$)
1998.3 (.05)	1977.4	1.011		$\Delta\nu_1=1$, $\Delta\nu_3=1$ or $\Delta\nu_3=2$ ($\tilde{X}\,^2\Sigma_u^+$)
			2052±40	$\Delta\nu_3=2$ ($\tilde{X}\,^2\Sigma_u^+$)
3330 (.08)	3259	1.022	3291±40	$\Delta\nu_3=3$ ($\tilde{X}\,^2\Sigma_u^+$)
4425 (.07)	4358	1.015		
5506 (.10)	5444	1.011		
5882 (.54)	5778	1.018	5888±40	$\Delta\nu_3=5$ ($\tilde{X}\,^2\Sigma_u^+$)
6123 (.60)	6074	1.008		

In the work presented here, we find no evidence for a low-lying cyclic (doublet) state at either the CCSD(T) or B3LYP levels of theory. In addition, the experimental spectra in combination with the calculated BD(T) ν_3 potential convincingly show that the ν_3 fundamental is surprisingly low (855 cm^{-1}). This is a result of the Herzberg–Teller coupling between the $\tilde{X}\,^2\Sigma_u^+$ ground state and the low-lying $\tilde{A}\,^2\Sigma_g^+$ excited state and is reflected in the highly nonharmonic nature of the antisymmetric stretch potential. Regarding isotope effects, the ν_3 frequency ratio should be 1.021 for $^{11}B^{14}N^{11}B$ and $^{11}B^{15}N^{11}B$ within the normal mode approximation. IR frequencies and ratios for $^{11}B^{14}N^{11}B$ and $^{11}B^{15}N^{11}B$ deposited in a matrix are listed in Table VI. The matrix peaks at 882.3, 3330, and 5882 cm^{-1} for $^{11}B^{14}N^{11}B$ show the expected ν_3 isotope effect and have the same spacing as the 3_0^1, 3_0^3, and 3_0^5 photodetachment transitions seen in the photoelectron spectrum. It therefore appears that these three infrared peaks are due to $\Delta\nu_3=1$, 3, and 5 vibrational transitions originating from the $\nu_i=0$ level of the $\tilde{X}\,^2\Sigma_u^+$ state of linear BNB, and not to cyclic BN_2. The anomalously large intensities of the two higher energy transitions is presumably brought about by vibronic coupling with the $\tilde{A}\,^2\Sigma_g^+$ state.

Several other peaks in the IR spectrum can also be assigned. The weak absorption peak at 1736.5 cm^{-1}, previously assigned to the fundamental of the ν_3 mode of linear neutral B–N–B, is reassigned to the fundamental of the ν_3 mode in the anion ground state $\tilde{X}\,^2\Sigma_u^+$ (1732 cm^{-1}). The signal at 1998.3 cm^{-1} in the absorption spectrum may either be assigned to the first overtone of the ν_3 mode (present study: $2052\pm40\,cm^{-1}$ or the combination band involving the fundamentals of the ν_1 and ν_3 modes. The latter transition should be forbidden, but this assignment is supported by the

frequency ratio of 1.011, which is intermediate between the corresponding ratios for the ν_3 mode (1.021) and the ν_1 mode (1.000). Finally, the gas phase term energy of the $\tilde{A}\,^2\Sigma_g^+$ state is 0.785 ± 0.005 eV ($6332 \pm 40\,\mathrm{cm}^{-1}$), too high to account for the intense absorption at 6123 cm^{-1} in the matrix, but this peak may be due to higher overtones of the ν_3 mode or combination bands.

VI. SUMMARY

The signal observed in the 355 and 266 nm photoelectron spectra of B_2N^- has been assigned to photodetachment from the anion ground state ($\tilde{X}\,^1\Sigma_g^+$) to the ground and lowest excited state of neutral B_2N ($\tilde{X}\,^2\Sigma_u^+$ and $\tilde{A}\,^2\Sigma_g^+$) with a linear, symmetric B–N–B geometry. The EA of B_2N is 3.098 ± 0.005 eV. The symmetric and antisymmetric stretching vibrations of these three states have been characterized. The spectra present strong evidence for Herzberg–Teller vibronic coupling between the $\tilde{X}\,^2\Sigma_u^+$ and $\tilde{A}\,^2\Sigma_g^+$ states along the antisymmetric stretch normal coordinate, manifested by the observation of FC forbidden transitions. Vibronic coupling also results in a strongly nonharmonic potential with exceptionally low eigenvalues for the ν_3 mode of the $\tilde{X}\,^2\Sigma_u^+$ state.

At the B3LYP/aug-cc-pVTZ and CCSD(T)/aug-cc-pVTZ level of theory the calculated adiabatic detachment energies are in good agreement with the experimental results. Harmonic frequencies and changes in equilibrium geometry between the anion and the neutral are predicted correctly, except for the antisymmetric stretching frequencies of the neutral states. The UHF, CCSD, CCSD(T), BD, and BD(T) wave functions display artifactual symmetry breaking along the antisymmetric stretch coordinate. Nonetheless, slightly modified forms of the BD(T) ν_3 potential quantitatively reproduce the experimentally determined eigenvalue spacing for the $\tilde{X}\,^2\Sigma_u^+$. The B3LYP wave function does not suffer from artifactual symmetry breaking but fails to reproduce quartic character of the ν_3 mode. The CCSD(T) and B3LYP calculations also agree well for the other two isomers of B_2N, linear B–B–N, and cyclic B_2N. Both models unambiguously predict linear B–N–B structures for the absolute minima on the anion and neutral ground state potential energy surface. The B3LYP and CCSD(T) calculations predict no minimum for a low-lying, cyclic $^2B_2$ state, which has been invoked in the interpretation of the matrix absorption spectrum.[12] On the basis of the present experimental and computational results the matrix absorption spectrum of B_2N is reassigned to the ground state of linear B–N–B.

ACKNOWLEDGMENTS

This research is supported by the National Science Foundation under Grant No. DMR-9814677. K.R.A. gratefully acknowledges a postdoctoral fellowship from the Swiss National Science Foundation. This research used resources of the National Energy Research Scientific Computing Center, which is supported by the Office of Science of the U.S. Department of Energy under Contract No. DE-AC03-76SF00098. Special appreciation is expressed to Professor Martin Head-Gordon, Dr. David Sherrill, Dr. Steve Gwaltney, and Dr. Stephan Matzinger for helpful discussions.

[1] P. B. Mirkarimi, K. F. McCarty, and D. L. Medlin, Mater. Sci. Eng. R. **21**, 47 (1997).
[2] A. E. Douglas and G. Herzberg, Can. J. Res. **18**, 179 (1940).
[3] B. A. Thrush, Nature (London) **186**, 1044 (1960).
[4] O. A. Mosher and R. P. Frosch, J. Chem. Phys. **52**, 5781 (1970).
[5] H. Bredohl, I. Dubois, Y. Houbrechts, and P. Nzohabonayo, J. Phys. B **17**, 95 (1984).
[6] H. Bredohl, I. Dubois, Y. Houbrechts, and P. Nzohabonayo, J. Mol. Spectrosc. **112**, 430 (1985).
[7] R. D. Verma, J. Phys. B **22**, 3689 (1989).
[8] M. Lorenz, J. Agreiter, A. M. Smith, and V. E. Bondybey, J. Chem. Phys. **104**, 3143 (1996).
[9] R. S. Ram and P. F. Bernath, J. Mol. Spectrosc. **180**, 414 (1996).
[10] K. R. Asmis, T. R. Taylor, and D. M. Neumark, Chem. Phys. Lett. **295**, 75 (1998).
[11] L. B. Knight, D. W. Hill, T. J. Kirk, and C. A. Arrington, J. Phys. Chem. **96**, 555 (1992).
[12] L. Andrews, P. Hassanzadeh, T. R. Burkholder, and J. M. L. Martin, J. Chem. Phys. **98**, 922 (1993).
[13] C. A. Thompson and L. Andrews, J. Am. Chem. Soc. **117**, 10125 (1995).
[14] C. A. Thompson, L. Andrews, J. M. L. Martin, and J. El-Yazal, J. Phys. Chem. **99**, 13839 (1995).
[15] S. Becker and H.-J. Dietze, Int. J. Mass Spectrom. Ion Processes **73**, 157 (1986).
[16] G. Seifert, B. Schwab, S. Becker, and H.-J. Dietze, Int. J. Mass Spectrom. Ion Processes **85**, 327 (1988).
[17] K. R. Asmis, T. R. Taylor, and D. M. Neumark, Eur. Phys. J. D (in press).
[18] J. M. L. Martin, J. P. François, and R. Gijbels, J. Chem. Phys. **90**, 6469 (1989).
[19] J. M. L. Martin, J. El-Yazal, J.-P. Francois, and R. Gijbels, Mol. Phys. **85**, 527 (1995).
[20] P. R. Taylor, J. M. L. Martin, J. P. François, and R. Gijbels, J. Phys. Chem. **95**, 6530 (1991).
[21] R. S. Grev, I. L. Alberts, and H. F. Schaefer III, J. Phys. Chem. **94**, 3379 (1990).
[22] R. B. Metz, A. Weaver, S. E. Bradforth, T. N. Kitsopoulos, and D. M. Neumark, J. Phys. Chem. **94**, 1377 (1990).
[23] C. Xu, G. R. Burton, T. R. Taylor, and D. M. Neumark, J. Chem. Phys. **107**, 3428 (1997).
[24] J. Cooper and R. N. Zare, J. Chem. Phys. **48**, 942 (1968).
[25] K. M. Ervin and W. C. Lineberger, in *Advances in Gas Phase Ion Chemistry*, edited by N. G. Adams and L. M. Babcock (JAI, Greenwich, CT, 1992), Vol. 1, pp. 121–166.
[26] M. J. Frisch, G. W. Trucks, M. Head-Gordon, P. M. W. Gill, M. W. Wong, J. B. Foresman, B. G. Johnson, H. B. Schlegel, M. A. Robb, E. S. Replogle, R. Gomperts, J. L. Andres, K. Raghavachari, J. S. Binkley, C. Gonzalez, R. L. Martin, D. J. Fox, D. J. Defrees, J. Baker, J. J. P. Stewart, and J. A. Pople, GAUSSIAN, Revision E.2 ed. (Gaussian, Inc., Pittsburgh, PA, 1992).
[27] M. J. Frisch, G. W. Trucks, H. B. Schlegel, P. M. W. Gill, B. G. Johnson, M. A. Robb, J. R. Cheeseman, T. Keith, G. A. Petersson, J. A. Montgomery, K. Raghavachari, M. A. Al-Laham, V. G. Zakrzewski, J. V. Ortiz, J. B. Foresman, J. Cioslowski, B. B. Stefanov, A. Nanayakkara, M. Challacombe, C. Y. Peng, P. Y. Ayala, W. Chen, M. W. Wong, J. L. Andres, E. S. Replogle, R. Gomperts, R. L. Martin, D. J. Fox, J. S. Binkley, D. J. Defrees, J. Baker, J. P. Stewart, M. Head-Gordon, C. Gonzalez, and J. A. Pople, GAUSSIAN, Revision E.1 ed. (Gaussian, Inc., Pittsburgh, PA, 1995).
[28] T. H. Dunning, Jr., J. Chem. Phys. **90**, 1007 (1989).
[29] R. A. Kendall, T. H. Dunning, Jr., and R. J. Harrison, J. Chem. Phys. **96**, 6796 (1992).
[30] C. Lee, W. Yang, and R. G. Parr, Phys. Rev. B **37**, 785 (1988).
[31] A. D. Becke, J. Chem. Phys. **98**, 5648 (1993).
[32] K. Raghavachari, G. W. Trucks, J. A. Pople, and M. Head-Gordon, Chem. Phys. Lett. **157**, 479 (1989).
[33] G. D. Purvis III and R. J. Bartlett, J. Chem. Phys. **76**, 1910 (1982).
[34] T. J. Lee and P. R. Taylor, Int. J. Quantum Chem. Symp. **23**, 199 (1989).
[35] G. S. Tschumper and H. F. Schaefer III, J. Chem. Phys. **107**, 2529 (1997).
[36] L. A. Curtiss, P. C. Redfern, K. Raghavachari, and J. A. Pople, J. Chem. Phys. **109**, 42 (1998).

[37] D. Feller and K. A. Peterson, J. Chem. Phys. **108**, 154 (1998).
[38] J. M. L. Martin, J. P. François, and R. Gijbels, Chem. Phys. Lett. **193**, 243 (1992).
[39] E. R. Davidson and W. T. Borden, J. Phys. Chem. **87**, 4783 (1983).
[40] P. O. Löwdin, Rev. Mod. Phys. **35**, 496 (1963).
[41] W. D. Allen, D. A. Horner, R. L. DeKock, R. B. Remington, and H. F. Schaefer III, Chem. Phys. **133**, 11 (1989).
[42] P. Y. Ayala and H. B. Schlegel, J. Chem. Phys. **108**, 7560 (1998).
[43] C. D. Sherrill, M. S. Lee, and M. Head-Gordon, Chem. Phys. Lett. **302**, 425 (1999).
[44] N. C. Handy, J. A. Pople, M. Head-Gordon, K. Raghavachari, and G. W. Trucks, Chem. Phys. Lett. **164**, 185 (1989).
[45] C. D. Sherrill, A. I. Krylov, E. F. C. Byrd, and M. Head-Gordon, J. Chem. Phys. **109**, 4171 (1998).
[46] C. E. Dykstra, Chem. Phys. Lett. **45**, 466 (1977).
[47] G. Herzberg and E. Teller, Z. Phys. Chem. (Leipzig) **21**, 410 (1933).
[48] K. M. Ervin and W. C. Lineberger, J. Phys. Chem. **95**, 1167 (1991).
[49] T. R. Taylor, C. Xu, and D. M. Neumark, J. Chem. Phys. **108**, 10018 (1998).
[50] F. Tarantelli, L. S. Cederbaum, and P. Campos, J. Chem. Phys. **91**, 7039 (1989).
[51] A. Schmelzer and E. Haselbach, Helv. Chim Acta **54**, 1299 (1971). The present improved version of the program has been written by T. Bally, S. Matzinger and B. Albrecht.